Int. J. Solids Structures, Vol. 18, No. 2, pp. 121–138, 1982
Printed in Great Britain.

0020-7683/82/020121-18$03.00/0
Pergamon Press Ltd.

ON THE DEVELOPMENT OF SHEAR BANDS IN PURE BENDING

N. TRIANTAFYLLIDIS† and A. NEEDLEMAN
Division of Engineering, Brown University, Providence, RI 02912, U.S.A.

and

V. TVERGAARD
Department of Solid Mechanics, The Technical University of Denmark, 2800 Lyngby, Denmark

(*Received* 12 *November* 1980; *in revised form* 6 *April* 1981)

Abstract—The development of shear bands in a plate subject to pure bending is analyzed numerically. For a plate with an initial periodic imperfection, the course of shear band development is determined for three material models; an elastic–plastic solid with a rather sharp vertex on its yield surface, an elastic–plastic solid with a more blunt vertex on its yield surface and a nonlinear elastic solid. The uniaxial stress–strain behavior of these material models is taken to be identical. In each case, the initial imperfection leads to the development of surface undulations on both the compressive and tensile sides of the plate and, subsequently, shear bands initiate at points of strain concentration induced by these surface undulations. The course of shear band development is found to depend on the constitutive law employed to characterize the material behavior. For the elastic–plastic solid with the sharper vertex, the effect of additional longer wavelength imperfections is considered. These additional long wavelength imperfections enhance the process of shear band development by focussing the deformation into one or a few shear bands. In pure bending, the shear bands must propagate into the plate against an adverse deformation gradient so that the peak straining within the bands always occurs at the free surface and the shear bands end inside the plate.

1. INTRODUCTION

Localization of plastic flow in narrow shear bands is frequently observed in ductile metals subject to tensile or compressive loading. The inception of localization has been analyzed for several material models, based on a theoretical framework due to Hadamard[1], Thomas[2] and Hill[3]. Such analyses consider a homogeneously deformed solid and determine the state at which bifurcation into a localized shear band is first possible. This bifurcation coincides with the loss of ellipticity of the governing incremental equations, Hill[3], Rice[4].

The growth of a shear band can be analyzed by a straightforward analysis[4] in cases where the stress state outside the band is homogeneous and the band is assumed to have constant width. However, in a solid subject to a non-uniform state of deformation the determination of shear band growth requires a much more elaborate analysis. The first loss of ellipticity at a point of the material and the corresponding directions of characteristics can be determined readily; but the growth of the localized shear deformations and the extent to which shear bands extend into neighboring elliptic regions of the material is a more complex question.

Some progress has been made by Tvergaard *et al.*[5] for the plane strain tensile test, in which diffuse necking occurs first and subsequently shear bands develop in the non-uniformly strained neck region. In [5] it was found that the locations of shear bands were very sensitive to the form of small initial surface imperfections. Also, the intensity of the localized shearing varied considerably along the bands, which often ended inside the material. The emergence of shear bands from a slight material imperfection inside an otherwise homogeneous body has been studied recently by Abeyaratne and Triantafyllidis[6]. Somewhat related to these results are the bands found by Knowles and Sternberg[7] and Abeyaratne[8] in the vicinity of the tip of a crack in anti-plane shear.

The present paper considers shear band development in a plate subject to pure bending. Interest in this problem stems from various metal forming processes involving bending of sheet metal, where bending beyond a certain minimum radius of curvature relative to the plate thickness can lead to shear fracture at the surface. The possibility of bifurcation away from the cylindrically symmetric fundamental state of pure bending has been studied by Triantafyllidis[9] for an incompressible nonlinear elastic solid. The critical bifurcation mode is

†Present address: Department of Aerospace Engineering, University of Michigan, Ann Arbor, MI 48109, U.S.A.

a surface wave mode, which occurs first in the compressive region, with the shortest possible wavelength being critical. Subsequently, if the fundamental unbifurcated state is thought to be continued beyond the first critical bifurcation point, ellipticity of the governing equations is lost at the surfaces. The directions of the characteristics in these hyperbolic surface regions are shown in [9]. However, as soon as the first bifurcation point is reached, the surface waves will start to grow, with very little additional overall straining being required to meet the condition for shear band inception in small material regions at the wave bottoms, Hutchinson and Tvergaard [10].

The particular material model to be used in the present investigation is the J_2 corner theory developed by Christoffersen and Hutchinson [11], which was also used in studies of the plane strain tensile test [5] and surface instabilities [10]. In the total loading regime, for nearly proportional loading, the instantaneous moduli are chosen as those of a nonlinear elastic solid (a large strain generalization of J_2 deformation theory). In the transition regime, for larger deviations from proportional loading, the moduli are taken to stiffen smoothly until they coincide with those of a linear elastic solid for stress increments directed along or within the yield surface corner. For comparison purposes some results employing the nonlinear elastic constitutive law are also included.

Bifurcation results based on the nonlinear elastic material model, as in [9], also hold for J_2 corner theory as long as deviations from proportional loading remain inside the total loading regime. For the bent plate this requirement is not satisfied since strong deviations from proportional loading occur in the prebifurcation state. However, near the surface regions that are most highly stressed and thus most important for bifurcation proportional loading does take place. In addition to this limitation on the validity of the nonlinear elastic bifurcation predictions, the subsequent growth of shear bands is quite sensitive to details of the vertex description, Hutchinson and Tvergaard [12]. In the limiting case of a classical elastic–plastic solid with a smooth yield surface, satisfying normality, there is strong resistance to shear band localization [13].

2. PROBLEM FORMULATION

We consider a plate, as depicted in Fig. 1(a), of length $2L_0$ and thickness $h_0+2\Delta h_0$ in the initial unstressed state, where h_0 is the average thickness and $2\Delta h_0$ is an initial thickness inhomogeneity. The plate is subjected to pure bending by rotating its ends through an angle 2θ relative to each other. Plane strain conditions are assumed to prevail throughout the deformation history.

A Lagrangian formulation of the field equations, see, e.g. [14, 15], is adopted which has been used extensively in previous finite element analyses [16–18, 10, 5, 6]. The initial unstressed configuration is taken as reference and a material point is identified by its Cartesian coordinates x^i in the reference state. The reference state metric tensor is denoted by g_{ij}, with determinant g, while in the current configuration the metric tensor is G_{ij} and the determinant is G. The Lagrangian strain tensor is given by

$$\eta_{ij}=\frac{1}{2}(G_{ij}-g_{ij})=\frac{1}{2}(u_{i,j}+u_{j,i}+u^k_{,i}u_{k,j}) \tag{1}$$†

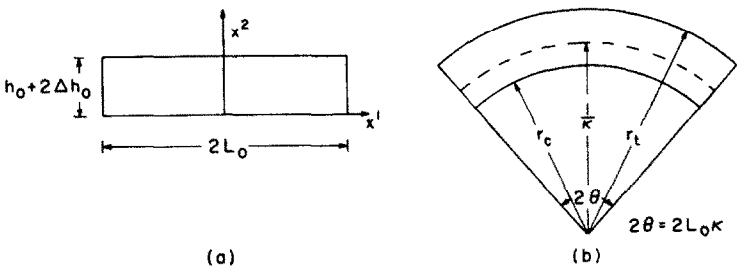

Fig. 1. (a) The undeformed configuration of a plate, (b) The bent configuration assumed by a perfect plate.

†Latin indices range from 1 to 3, while Greek indices, which will be employed subsequently, range from 1 to 2.

where u^k are the displacement components on the reference base vectors and $(\ )_{,i}$ denotes covariant differentiation in the reference coordinate system.

Equilibrium is expressed by the principle of virtual work which, under plane strain conditions, is given by

$$\int_A \tau^{\alpha\beta}\delta\eta_{\alpha\beta}\,dA = \int_s T^\alpha \delta u_\alpha\,ds. \tag{2}$$

Here, A and s denote, respectively, the cross-sectional area and perimeter of the body in the reference configuration, $\tau^{\alpha\beta}$ are the contravariant components of the Kirchoff stress tensor on the embedded deformed coordinates and T^α are the components of the nominal traction vector on the reference base vectors.

The contravariant components $\tau^{\alpha\beta}$ of the Kirchhoff stress tensor are related to the corresponding components of the Cauchy stress tensor $\sigma^{\alpha\beta}$ by

$$\tau^{\alpha\beta} = \sqrt{(G/g)}\,\sigma^{\alpha\beta} \tag{3}$$

and the nominal traction components on a curve with normal n_β in the reference configuration are given by

$$T^\alpha = (T^{\alpha\beta} + \tau^{\gamma\beta}u^\alpha_{,\gamma})n_\beta. \tag{4}$$

An identity related to the principle of virtual work (2), which will prove useful in the subsequent analysis, is

$$\int_A \tau^{\alpha\beta}(u^*_{\alpha,\beta} + u^\gamma_{,\alpha}u^*_{\gamma,\beta})\,dA = \int_s T^\alpha u^*_\alpha\,ds \tag{5}$$

where $\tau^{\alpha\beta}$ and u_α are the equilibrium stress and displacement fields at a given stage of the deformation history and u^*_α is any conveniently chosen compatible displacement field.

Consideration is restricted to deformations symmetrical about the center line of the plate, $x^1 = 0$ in Fig. 1(a), so that only one-half of the plate needs to be considered in the numerical solution. The symmetry conditions are expressed by

$$u_1 = 0, \quad T^2 = 0 \quad \text{at} \quad x^1 = 0. \tag{6}$$

The top and bottom surfaces of the plate are required to remain traction free so that

$$\begin{aligned} T^1 = T^2 = 0 \quad &\text{at} \quad x^2 = -\Delta h_0 \\ T^1 = T^2 = 0 \quad &\text{at} \quad x^2 = h_0 + \Delta h_0. \end{aligned} \tag{7}$$

The initial thickness inhomogeneity, Δh_0, is specified by

$$\Delta h_0 = h_0\left[\bar{\xi}_1 \cos\frac{m_1\pi x^1}{L_0} + \bar{\xi}_2 \cos\frac{m_2\pi x^1}{L_0}\right] \tag{8}$$

where $\bar{\xi}_1$ and $\bar{\xi}_2$ are imperfection amplitudes and m_1 and m_2 are the corresponding wave numbers.

The edge of the plate $x^1 = L_0$ is rotated through an angle θ relative to the center line $x^1 = 0$ while remaining shear free. Taking the point about which the line $x^1 = L_0$ rotates to be $x^2 = h_0/2$, the current Cartesian coordinates, $\bar{x}^1$ and $\bar{x}^2$, of points on this line are related by

$$\frac{\bar{x}^1 - L_0}{\bar{x}^2 - \frac{1}{2}h_0} = \tan\theta. \tag{9}$$

Rewriting (9) in terms of the displacement components u^α gives the boundary conditions on the edge of the plate as

$$\left.\begin{array}{c} -u^1\cot\theta + u^2 = -x^2 + (1/2)h_0 \\ T^2\cos\theta + T^1\sin\theta = 0 \end{array}\right\} \text{at } x^1 = L_0. \tag{10}$$

We have chosen to express the first of eqns (10) in terms of the cotangent function, rather than in terms of the tangent function in order to avoid numerical difficulties at $\theta = \pi/2$. Initially, at $\theta = 0$ numerical difficulties are avoided by using the first of eqns (10) multiplied by $\tan\theta$.

In interpreting some of the numerical solutions, advantage will be taken of the fact that the boundary conditions imposed here on the edges $x^1 = 0$ and $x^1 = L_0$ are also the appropriate symmetry conditions for a segment of a plate of initial length $2kL_0$ ($k = 1, 2, 3\ldots$). The ends of the plate are rotated through an angle $2k\theta$ relative to each other, while requiring the deformations to be periodic in the x^1-direction with period $2L_0$. Within each segment, $(i-1)L_0 \le x^1 \le (i+1)L_0$, $i = -(k-1)$ to $(k-1)$, the deformations are presumed symmetric about the midpoint $x^1 = iL_0$.

3. CONSTITUTIVE RELATIONS

The constitutive relation employed here is the J_2 corner theory of Christoffersen and Hutchinson[11]. This theory was introduced in order to develop an analytically tractable phenomonological theory of plasticity which would incorporate certain features exhibited by physical theories of plasticity. Quite generally, in physical models of polycrsytalline aggregates, based on single crystal slip, the discreteness of slip systems in each grain leads to the prediction of a yield surface vertex at the current loading point, when the yield surface is defined for small offset plastic strains[19]. Calculations carried out for specific polycrystalline models do exhibit yield surface vertices[20, 21], although experimental evidence for the formation of such vertices is ambiguous and conflicting[22].

The significance of vertex formation for bifurcation related phenomena in the plastic range has been long appreciated in the context of plastic buckling applications[23, 24]. Recently, the destabilizing effect of a vertex in tensile bifurcations has been investigated in a variety of problems by employing some finite strain generalization of the J_2 deformation theory of plasticity. When the bifurcation state involves a proportional or nearly proportional loading history, deformation theory is an acceptable plasticity theory for analyzing the onset of bifurcation. However, even in these problems deformation theory is not an acceptable plasticity theory for addressing questions concerning post-bifurcation behavior and imperfection sensitivity, since strongly nonproportional loading almost always occurs in the post-bifurcation regime. In the particular problem considered here, deformation theory is not even an appropriate plasticity theory for investigating the onset of bifurcation due to the fact that strong deviations from proportional loading take place well before the onset of bifurcation.

In J_2 corner theory the instantaneous moduli for nearly proportional loading are chosen to be the moduli of J_2 deformation theory and for increasing deviation from proportional loading the moduli stiffen monotonically until they coincide with the linear elastic moduli for stress rates directed along or within the corner of the yield surface. With M^0_{ijkl} denoting the deformation theory compliances and M_{ijkl} denoting the linear elastic compliances, the plastic compliances of deformation theory are $C_{ijkl} = M^0_{ijkl} - M_{ijkl}$ so that

$$\dot\eta^p_{ij} = C_{ijkl}\overset{\nabla}{\tau}{}^{kl}. \tag{11}$$

Here, $\dot\eta^p_{ij}$ is the plastic part of the strain rate, $\overset{\nabla}{\tau}{}^{kl}$ are the Jaumann rates of the contravariant Kirchhoff stress components and by rate is meant differentiation with respect to some monotonically increasing parameter which characterizes the deformation history.

The yield surface in the neighborhood of the current loading point is taken to be a cone in stress deviator space with the cone axis in the direction

$$\lambda^{ij} = s^{ij}(C_{mnpq}s^{mn}s^{pq})^{-1/2} \tag{12}$$

where the stress deviator $s^{ij} = \tau^{ij} - 1/3G_{kl}\tau^{kl}G^{ij}$.

An angular measure θ† of the stress rate direction relative to the cone axis is defined by

$$\cos\theta = C_{ijkl}\lambda^{ij}\overset{\nabla}{s}{}^{kl}(C_{mnpq}\overset{\nabla}{s}{}^{mn}\overset{\nabla}{s}{}^{pq})^{-1/2}. \tag{13}$$

The stress rate potential at the vertex is given by

$$W = \frac{1}{2}M_{ijkl}\overset{\nabla}{\tau}{}^{ij}\overset{\nabla}{\tau}{}^{kl} + \frac{1}{2}f(\theta)C_{ijkl}\overset{\nabla}{\tau}{}^{ij}\overset{\nabla}{\tau}{}^{kl}. \tag{14}$$

The transition function $f(\theta)$ is unity throughout the total loading range, which is specified by $0 \le \theta \le \theta_0$ and is identically zero for $\theta_c < \theta \le \pi$, where θ_c denotes the angle of the yield surface cone. In the transition regime, $\theta_0 \le \theta \le \theta_c$, $f(\theta)$ decreases monotonically and smoothly from unity to zero in a manner that ensures convexity of the incremental relation. The transition function employed here is the same as that employed in [5, 10] and is specified by

$$f(\theta) = \frac{1}{g(\phi)[1 + l^2(\phi)]} \tag{15}$$

where

$$\theta(\phi) = \phi + \arctan[l(\phi)], \quad l(\phi) = \frac{dg/d\phi}{2g(\phi)} \tag{16}$$

and

$$g(\phi) = \begin{cases} 1 & 0 \le \phi \le \theta_0 \\ \{1 - [(\phi - \theta_0)/(\theta_n - \theta_0)]^3\}^{-2}, & \theta_0 \le \phi \le \theta_n \end{cases} \tag{17}$$

with $\theta_n = \theta_c - \pi/2$. Of the transition functions considered in [11], this transition function was found to most closely duplicate the moduli found in [20] using a self-consistent model of a polycrsytalline aggregate. From the potential function (14) the strain rate is found to be

$$\dot{\eta}_{ij} = \frac{\partial^2 W}{\partial\overset{\nabla}{\tau}{}^{ij}\partial\overset{\nabla}{\tau}{}^{kl}}\overset{\nabla}{\tau}{}^{kl} = M_{ijkl}(\theta)\overset{\nabla}{\tau}{}^{kl}. \tag{18}$$

Inverting (18) gives the moduli $R^{ijkl}(\theta)$ relating the Jaumann rate of Kirchhoff stress and the strain rate so that

$$\overset{\nabla}{\tau}{}^{ij} = R^{ijkl}(\theta)\dot{\eta}_{kl}. \tag{19}$$

In J_2 corner theory the total loading moduli are taken to be those of some finite strain version of small strain J_2 deformation theory. As in [5], we employ the incremental moduli of a nonlinear elastic solid to give the J_2 corner theory total loading moduli. The principal axes techniques of Hill[25–27] are used to determine the components of the tensor of moduli **R** on the Eulerian principal axes, giving

$$\begin{aligned} R_{ijkl} &= 2G_s\left[\delta_{ik}\delta_{jl} + \frac{\nu_s}{1-2\nu_s}\delta_{ij}\delta_{kl} - \frac{3}{2}\frac{E_s/E_t - 1}{E_s/E_t - \dfrac{1-2\nu_s}{3}}\frac{s_{ij}s_{kl}}{\sigma_e^2}\right] \text{ for } i = j,\ k = l \\ R_{1212} &= R_{2121} = R_{1221} = R_{2112} = G_s q \quad q = (\epsilon_1 - \epsilon_2)\coth(\epsilon_1 - \epsilon_2) \end{aligned} \tag{20}$$

where δ_{ij} is the Kronecker delta, ϵ_i are the logarithms of the principal stretches and $\sigma_e^2 =$

†The vertex angle θ which will only appear in this Section is in no way related to the angle θ, through which the plate is bent. The notation for vertex parameters employed here conforms with the notation in [11].

$3/2 s_{ij}s_{ij}$, s_{ij} being the Kirchhoff stress deviator on the principal axes. Furthermore, E_t is the slope of the uniaxial Kirchhoff stress–logarithmic strain curve, E_s is the ratio of stress to strain on this uniaxial stress strain curve and the parameters ν_s and G_s are defined by

$$\nu_s = 1/2 + E_s/E(\nu - 1/2), \quad G_s = E_s/2(1+\nu_s) \tag{21}$$

with E being Young's modulus and ν Poisson's ratio. With $q = 1$, (20) and (21) give the tensor of instantaneous moduli for the hypoelastic solid of Stören and Rice [28].

In addition to characterizing the response of the J_2 corner theory solid in the total loading regime, the nonlinear elastic solid having the incremental moduli (20) will be considered in its own right in some of the numerical results to be presented subsequently. The incremental relation (20) can be integrated to give the total Kirchhoff stress–logarithmic strain relation as

$$\tau_i = 2G_s\left[\epsilon_i + \frac{\nu_s}{1-2\nu_s}(\epsilon_1+\epsilon_2+\epsilon_3)\right] \tag{22}$$

and a strain energy function $\Phi = \Phi(\epsilon_1, \epsilon_2, \epsilon_3)$ can be constructed for which $\tau_i = \partial\Phi/\partial\epsilon_i$. As is more traditional in nonlinear elasticity theory, this strain energy function can also be expressed in terms of the strain invariants [6, 29].

The uniaxial Kirchhoff stress–logarithmic strain curve is represented by a piecewise power hardening law of the form

$$\begin{aligned} \tau &= E\epsilon & \tau &< \sigma_y \\ \tau/\sigma_y &= (\epsilon/\epsilon_y)^N & \tau &\geq \sigma_y \end{aligned} \tag{23}$$

where σ_y is the initial yield (Kirchhoff) stress, $\epsilon_y = \sigma_y/E$, and N is the strain hardening exponent.

For J_2 corner theory a more convenient measure of the yield surface angle than θ_c is the angle β_c given by

$$\tan\beta_c = -\frac{\sigma_y}{(\sigma_e^2 - \sigma_y^2)^{1/2}} \tag{24}$$

The angular measures θ_c and β_c are related by

$$\tan\theta_c = \sqrt{a}\tan\beta_c \quad a = \left[\frac{E}{E_s q} - 1\right]\left[\frac{E}{E_t} - 1\right]^{-1} \tag{25}$$

and q is defined in (20). Here, the sharpness of the cone angle is limited by employing (24) to give β_c for $\pi/2 \leq \beta_c \leq (\beta_c)_{\max}$ and taking $\beta_c = (\beta_c)_{\max}$ otherwise.

The components of the moduli **R** on the embedded deformed coordinates can be computed from the components on the principal axes by making use of standard kinematic relations. However, the Lagrangian formulation employed in the numerical calculations makes use of the relation between the convected rate of the contravariant components of Kirchhoff stress $\dot{\tau}^{\alpha\beta}$ and the Lagrangian strain rate $\dot{\eta}_{\gamma\delta}$ given in the form

$$\dot{\tau}^{\alpha\beta} = L^{\alpha\beta\gamma\delta}(\theta)\dot{\eta}_{\gamma\delta}. \tag{26}$$

The moduli **L** are obtained from the moduli **R** appearing in (19) by employing the relation

$$\dot{\tau}^{\alpha\beta} = \overset{\nabla}{\tau}{}^{\alpha\beta} - G^{\alpha\gamma}\tau^{\beta\delta}\dot{\eta}_{\gamma\delta} - G^{\beta\gamma}\tau^{\alpha\delta}\dot{\eta}_{\gamma\delta}. \tag{27}$$

4. BEHAVIOR OF A PERFECT PLATE IN PURE BENDING

We consider the behavior of a perfect ($\Delta h_0 \equiv 0$) incompressible plate subject to pure bending as imposed by the boundary conditions (6), (7) and (10). The slight degree of compressibility

included in the formulation on which the finite element results are based has little effect on the overall behavior.

One possible equilibrium configuration for the incompressible perfect plate is a portion of a cylinder as illustrated in Fig. 1(b). The principal stretches of a material point at a distance r from the current center of curvature of the plate are given by

$$\lambda_1 = \kappa r \quad \lambda_2 = 1/\kappa r. \tag{28}$$

Here, κ is the curvature of the currently unstretched fiber and the subscripts 1 and 2 denote principal values associated with the tangential and radial (through-the-thickness) directions, respectively. The current coordinate r of a material point is given in terms of the Cartesian coordinate x^2 in the reference configuration and the radius of the outer fiber under compression, r_c, via the incompressibility condition

$$r^2 - r_c^2 = 2x^2 h_0/(\kappa h_0). \tag{29}$$

The angle θ through which the plate has been bent is given in terms of the curvature κ, the initial thickness, h_0, and the initial length, L_0, by

$$\theta = (\kappa h_0)(L_0/h_0). \tag{30}$$

The deformations in this prebifurcation state, given by (28) and (29), are independent of the coordinate x^1 and are parameterized by the nondimensional curvature κh_0. Here, κh_0 will be chosen as the monotonically increasing parameter characterizing the deformation history. For a plate of initial length $2L_0$, the angle θ can be calculated from (30). When $\theta = \pi$, i.e. when $\kappa h_0 = \pi h_0/l_0$, the plate has been bent into a circular cylinder.

The complete solution for the deformation state, which involves solving for r_c as a function of the curvature κh_0, requires specification of the constitutive law, since the condition that the principal stress in the radial direction, σ_2, vanishes at the outer fibers is used to determine r_c.

For a nonlinear elastic material the general solution for the stress state has been obtained by Rivlin[30] and is explicitly given for the nonlinear elastic constitutive law (22), with piecewize power law hardening (23), by Triantafyllidis[9]. Integrating the analytical expression for the principal stress in the tangential direction, σ_1, given in [9] through the plate thickness gives the moment per unit width in the x^3-direction, M, i.e.

$$M = \int_{r_c}^{r_t} \sigma_1 r \, dr \tag{31}$$

where r_c is the radius of the outer fiber under compression and r_t is the radius of the outer fiber under tension as shown in Fig. 1(b). Figure 2 depicts the moment, M, as a function of the curvature, κh_0, for $N = 0.1$ and $\sigma_y/E = 0.002$. The moment reaches a maximum at $\kappa h_0 = 0.48$.

Also shown in Fig. 2 is the moment curvature relation for an elastic–plastic solid with

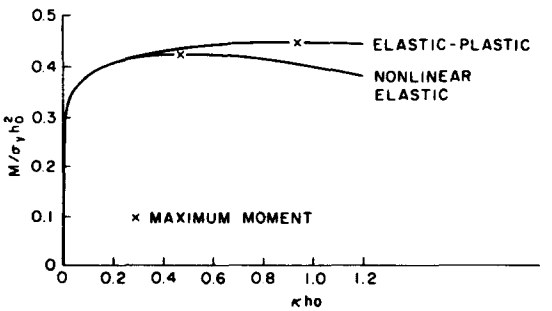

Fig. 2. The moment, M, vs curvature, κh_0, relations for incompressible perfect elastic–plastic and nonlinear elastic plates with $N = 0.1$ and $\sigma_y/E = 0.002$.

$N = 0.1$ and $\sigma_y/E = 0.002$. For an incompressible elastic–plastic solid the moment curvature relation depends on the uniaxial stress–strain curve, but not on the vertex characteristics, since at each material point the stress state is one of plane strain tension or compression with a superposed hydrostatic stress. In particular, the moment curvature relation shown in Fig. 2 for the elastic–plastic solid holds for the classical smooth yield surface plasticity theory with isotropic hardening as well as for the J_2 corner theory solid. The elastic–plastic results were obtained by a linear incremental method, with an iterative scheme being employed within each increment to ensure that $\sigma_2(r_c) = 0$ as well as $\sigma_2(r_t) = 0$.

Although the stress state at each material point is one of plane strain tension or compression, strongly nonproportional loading does occur. Initially, the unstretched fiber is at the center of the plate. As the curvature increases, the unstretched fiber moves toward the compressive side of the plate, as indicated schematically in Fig. 1(b), which leads to unloading occurring as the unstretched fiber propagates into material that has previously yielded. The solutions for the stress and deformation states for the elastic–plastic and nonlinear elastic solids coincide prior to the onset of unloading which occurs at $\kappa h_0 = 0.083$ for $\sigma_y/E = 0.002$ [9]. Even though unloading initiates quite early in the deformation history the moment vs curvature curves in Fig. 2 are indistinguishable to about $\kappa h_0 = 0.3$. Thereafter, the stiffening effect of unloading manifests itself and, for the elastic–plastic solid, a maximum moment is not reached until $\kappa h_0 = 0.93$. This maximum moment is 4.5% higher than the maximum moment attained by the nonlinear elastic solid.

As illustrated in Fig. 3, the strain histories at the most highly strained material points differ for the nonlinear elastic solid and the elastic–plastic solid. Plotted in this figure are the principal logarithmic strains in the tangential direction, $\epsilon_1 = \ln \lambda_1$, at the outer most fibers, $r = r_c$ and $r = r_t$, as a function of curvature κh_0. At the outermost compressive fiber, $r = r_c$, ϵ_1 is negative, while at the outermost tensile fiber, $r = r_t$, ϵ_1 is positive. For the nonlinear elastic solid, $\epsilon_1(r_c) = -\epsilon_1(r_t)$ [9]. For the elastic–plastic solid the magnitude of the strain is greater at the outermost compressive fiber than at the outermost tensile fiber.

Bifurcations from this state of pure bending, for the case of nonlinear elastic material behavior, have been considered by Triantafyllidis [9]. The bifurcation mode encountered at the lowest critical curvature corresponds to a short wavelength surface mode along the compressed ($r = r_c$) surface of the plate. At a somewhat higher curvature, a short wavelength surface mode along the stretched surfaces ($r = r_t$) of the plate becomes available. For a power hardening nonlinear elastic solid, the critical condition for the onset of a surface instability is [10]

$$\epsilon_1(1 - e^{-2\epsilon_1}) = N. \tag{33}$$

With $N = 0.1$, surface modes become available at $\epsilon_1 = -0.202$ (compression) and at $\epsilon_1 = 0.252$ (tension), corresponding to critical curvatures, κh_0, of 0.41 and 0.53, respectively. The critical curvature for the compressive surface waves occur prior to the maximum moment while that for tensile surface waves occurs after the maximum moment has been achieved.

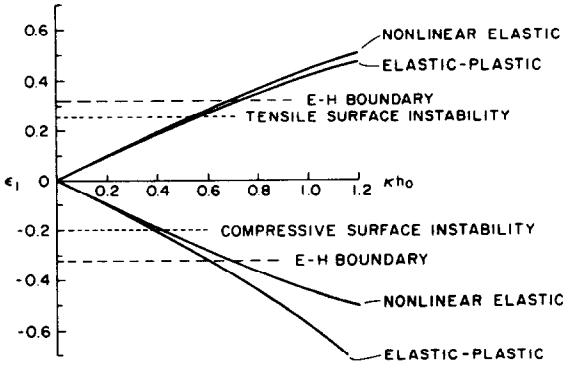

Fig. 3. The principal logarithmic strain in the tangential direction at the outermost fibers, ϵ_1, as a function of curvature, κh_0, for incompressible perfect elastic–plastic and nonlinear elastic plates with $N = 0.1$ and $\sigma_y/E = 0.002$.

At somewhat greater strains the outermost fibers are deformed to the point at which the incremental equilibrium equations admit real characteristics, that is, locally these equations become hyperbolic rather than elliptic. In the pure bending problem elliptic and hyperbolic regimes can coexist in different parts of the plate since the stress state is a function of position through the thickness[9]. Also, as exhibited in [9] the characteristics are curved. For the nonlinear elastic solid considered here, with power law hardening, the strain at the elliptic-hyperbolic interface is given by[12]

$$\epsilon_1^2 = N(q - N) \tag{34}$$

where q is defined in (20). With $N = 0.1$, (34) gives $\epsilon_1 = \pm 0.322$. As seen in Fig. 3, this strain is attained in the outermost fibers when $\kappa h_0 = 0.69$. Note that for the nonlinear elastic solid, ellipticity is lost at both the compressive and tensile surfaces at this critical curvature.

Since unloading occurs in the pure bending solution, Triantafyllidis bifurcation results[9] are not directly applicable for the J_2 corner theory solid. Nevertheless, it appears reasonable to presume that the critical condition for surface modes as well as for loss of ellipticity is a local one, to be satisfied at the surfaces $r = r_c$ and $r = r_t$. For the J_2 corner theory solid with a nonvanishing total loading regime ($\theta_0 > 0$), the critical strains for surface waves and shear bands are also given by (33) and (34). Even though the plane strain pure bending solution given by the classical smooth yield surface elastic–plastic solid with isotropic hardening coincides with that for the J_2 corner theory solid, the critical strains corresponding to surface waves and loss of ellipticity for the smooth yield surface case are much in excess of those given by (33) and (34) since these modes involve a change in loading path from the state of plane strain tension or compression.

As can be seen in Fig. 3, the curvatures at which the surface wave bifurcations and loss of ellipticity occur differ from the corresponding curvatures for the nonlinear elastic solid. The critical strain for surface waves in compression is reached at $\kappa h_0 = 0.39$ and in tension at $\kappa h_0 = 0.54$. These critical curvatures differ only slightly from the corresponding critical curvatures for the nonlinear elastic solid. However, loss of ellipticity in the pure bending state at the compressive surface occurs at a smaller curvature, $\kappa h_0 = 0.60$, for the elastic–plastic solid than for the nonlinear elastic solid. The loss of ellipticity in the pure bending state at the tensile surface is delayed somewhat, to $\kappa h_0 = 0.72$. For the J_2 corner theory solid the compressive and tensile surface wave bifurcations and the loss of ellipticity at the compressive and tensile outermost fibers all occur prior to the attainment of the maximum moment.

5. NUMERICAL METHOD AND RESULTS

Let the values of displacements, strains, stresses and tractions corresponding to a known approximate equilibrium state be given. The governing equations for prescribed increments of traction or displacement are obtained by expanding the principle of virtual work (2) about this state, which gives to lowest order,

$$\int_A [L^{\alpha\beta\gamma\delta}\dot{\eta}_{\alpha\beta}\delta\eta_{\gamma\delta} + \tau^{\alpha\beta}\dot{u}^{\gamma}_{,\alpha}\delta u_{\gamma,\beta}]\,dA = \int_s \dot{T}^{\alpha}\delta u_{\alpha}\,ds + \left[\int_s T^{\alpha}\delta u_{\alpha}\,ds - \int_A \tau^{\alpha\beta}\delta\eta_{\alpha\beta}\,dA\right] \tag{35}$$

where the moduli $L^{\alpha\beta\gamma\delta}$ are those appearing in (26) and $(\dot{\ })$ denotes increments of field quantities.

A similar expansion of the displacement constraint along $x^1 = L_0$ given in (10) yields

$$-\dot{u}^1\cot\theta + \dot{u}^2 = -\frac{u^1\dot{\theta}}{\sin^2\theta} + \left[u^1\cot\theta - u^2 - x^2 + \frac{1}{2}h_0\right]. \tag{36}$$

The incremental principle of virtual work (35) serves as the basis for implementing the numerical procedures. The finite element methods used in this study are those employed by Tvergaard, Needleman and Lo[5] suitably modified to accommodate the boundary constraint (36).

For a flow theory of plasticity such as J_2 corner theory, the equilibrium solution is path

dependent and a linear incremental procedure is used for this material model. At each stage of the computation the correction terms, the bracketed terms on the right hand sides of (35) and (36), are included to prevent drifting of the solution away from the true equilibrium path. For the path independent nonlinear elastic solid (35) is solved iteratively by the Newton–Raphson method to compute the equilibrium state exactly, within the limits of the chosen discretization. As will be shown subsequently, for a nonlinear elastic solid, the angle θ is not monotonically increasing along the equilibrium path. The mixed finite element-Rayleigh–Ritz method, Tvergaard[17], is employed, as in [5], to overcome numerical difficulties associated with this phenomenon.

Identical finite element discretizations are used for both material models. The grids consist of quadrilaterals made up of four constant strain triangular subelements which are formed by the two diagonals of the quadrilateral. For each quadrilateral static condensation is employed to eliminate the nodal degrees of freedom associated with the central node.

The grid was designed utilizing the prebifurcation solution given in [9]. A variable mesh spacing in the x^2-direction was chosen so that for a perfect incompressible nonlinear elastic plate a uniform element thickness would result at the critical curvature for shear bands. Furthermore, the length of the elements in the x^1-direction was adjusted to ensure, at bifurcation into the shear band mode, orientation of the diagonals of the top and bottom rows of elements along the most favorable angle for shear bands. Although, as noted in Section 4, the critical curvature for shear bands for the elastic–plastic plate differs from that for a nonlinear elastic plate, we employed the same mesh in the elastic–plastic calculations as in the nonlinear elastic calculations. In any case, due to the presence of the initial thickness imperfection (8), the conditions on mesh spacing and orientation at the onset of shear band development discussed above are only met approximately for an imperfect plate. Typical undeformed meshes are shown in Figs. 10 and 12.

In all the calculations reported on here, the uniaxial stress–strain behavior of the material is characterized by a yield strain, σ_y/E, of 0.002, a Poisson's ratio, ν, of 0.3 and a strain hardening exponent, N, of 0.1 and 32 elements are employed through the plate thickness.

We first consider a plate with a periodic imperfection in the x^1-direction, and focus attention on the growth of one half-wavelength. The half-wavelength to thickness ratio is 0.301 and the initial imperfection is specified by setting $m_1 = 1$, $\bar{\xi}_1 = 6 \times 10^{-4}$ and $\bar{\xi}_2 \equiv 0$ in (8).

Figure 4 displays the computed moment vs curvature curves for three material models; the nonlinear elastic solid, a J_2 corner theory solid with a limiting cone angle, $(\beta_c)_{max}$, of 135° and a J_2 corner theory solid with a more blunt limiting cone angle of 115°. The angle limiting the total loading range, θ_0, is taken as $\theta_0 = \theta_c/2 - \pi/4$ with θ_c given by (25). The vertex characterization with $(\beta_c)_{max} = 135°$ was also employed in [5], while Hutchinson and Tvergaard [12] compared the course of shear band development in homogeneous plane strain tension for the two vertex characterizations employed here.

Plotted in Fig. 4 is the moment, M, calculated from (5) with a suitable choice of $\mathbf{u}^*$ and normalized by $\sigma_y h_0^2$, against the curvature parameter κh_0. For an imperfect plate κh_0 is defined in terms of the angle θ by (30). The curvature at which the maximum moment, M_{max}, is attained depends somewhat on the vertex description, with M_{max} occurring at $\kappa h_0 = 0.77$ for the vertex with $(\beta_c)_{max} = 115°$ and at $\kappa h_0 = 0.72$ for the vertex with $(\beta_c)_{max} = 135°$. In each case the

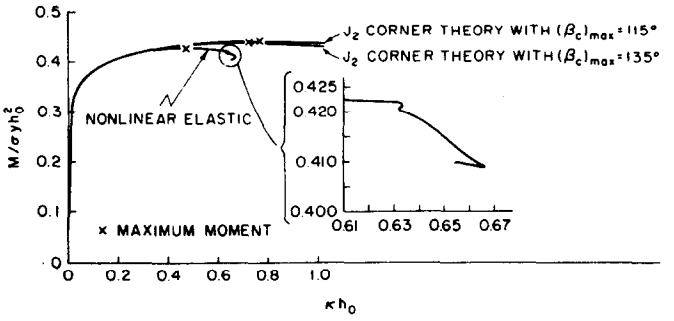

Fig. 4. The moment, M, vs curvature, κh_0, relations for plates with the initial thickness inhomogeneity specified by $\bar{\xi}_1 = 0.0006$, $m_1 = 1$ and $\bar{\xi}_2 = 0$ in (8), with a half wavelength to initial thickness ratio of 0.301.

maximum moment occurs at a significantly smaller curvature than for the perfect elastic–plastic plate depicted in Fig. 2. On the other hand, the moment-curvature relation for the imperfect nonlinear elastic plate is virtually identical with the one corresponding to a perfect plate until $\kappa h_0 \simeq 0.63$. Then the curvature κh_0, or equivalently the angle θ, ceases to increase monotonically. This nonmonotonic behavior is associated with the formation of shear bands, first on the compressive side and then on the tensile side of the plate.

The development of the deformation pattern is shown in Fig. 5, for the J_2 corner theory solids, and in Fig. 7 for the nonlinear elastic solid. These figures depict the deformed finite element mesh (only the quadrilaterals are shown) for a plate with an initial length, L_0, five times the half-wavelength of the initial imperfection. This choice of L_0, $L_0 = 1.51$, is made to facilitate comparison with results to be presented subsequently. We reiterate that the periodicity evident in these figures is enforced by the computation, since only one half wavelength is analyzed numerically.

In Fig. 5, at a curvature $\kappa h_0 = 0.31$, there is no evident deviation from the cylindrical deformation pattern of a perfect plate. At $kh_0 = 0.71$, which is somewhat prior to the attainment of the maximum moment, surface undulations are visible on both the compressive and tensile sides of the plate. The undulations on the compressive side are a bit more evident than those on the tensile side as could be anticipated from the fact that compressive surface waves begin to grow at a smaller curvature than do tensile surface waves. At this stage, the deformation patterns for the two corner descriptions are not visibly different. On the other hand, when $\kappa h_0 = 1.02$, a shear band pattern is evident in Fig. 5, with noticeably greater shearing for the solid with the sharper corner.

Figure 7 depicts deformation patterns at four stages of the loading history for the nonlinear elastic solid. Figure 7(a) is a stage early in the deformation history and the surfaces of the plate still appear cylindirical while Fig. 7(b), $\kappa h_0 = 0.626$, is well beyond the curvatures corresponding to compressive and tensile surface instabilities and both surface imperfections have been activated. At a slightly greater curvature $\kappa h_0 = 0.632$, the first snap back of the moment-curvature curve has occurred and shear bands have appeared at the compressive side of the plate. The final stage shows well developed shear bands on both surfaces, with increasing shearing occurring as the curvature decreases.

Figures 6 and 8 give a more quantitative picture of shear band development. In these figures contours of constant maximum principal strain are plotted in the current deformed configuration. Figures 6 and 8 depict the same stages of deformation as shown in Figs. 5 and 7, respectively. In these figures only one half the plate is pictured.

At the smallest curvatures, $\kappa h_0 = 0.31$ in Fig. 6 and $\kappa h_0 = 0.30$ in Fig. 8, a slight waviness of the contours, induced by the presence of the initial thickness imperfection, is evident. When the critical strain for surface waves has been passed, the waviness of the strain pattern grows rapidly. In Figs. 6(b_1) and 6(b_2) and in Fig. 8(b), the wavelength of the contour line for 0.30 is one third the wavelength of the initial imperfection on the compressive side of the plate and is equal to the wavelength of the initial imperfection on the tensile side of the plate.

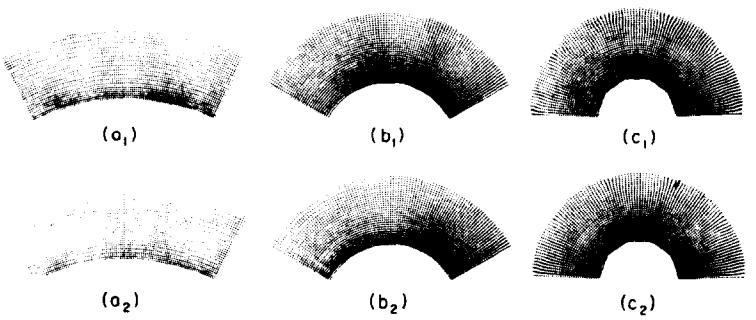

Fig. 5. The deformed mesh at three curvatures for the two vertex characterizations employed here. (a) $\kappa h_0 = 0.31$, (b) $\kappa h_0 = 0.71$, and (c) $\kappa h_0 = 1.02$. The subscript 1 refers to the vertex characterized by $(\beta_c)_{max} = 135°$ and the subscript 2 refers to the vertex characterized by $(\beta_c)_{max} = 115°$. The initial imperfection is specified by $\bar{\xi}_1 = 0.0006$, $m_1 = 1$ and $\bar{\xi}_2 = 0$ in (8), with a half wavelength to initial thickness ratio of 0.301. The configuration shown is for a plate five wavelengths long, but only one half wavelength was analyzed numerically.

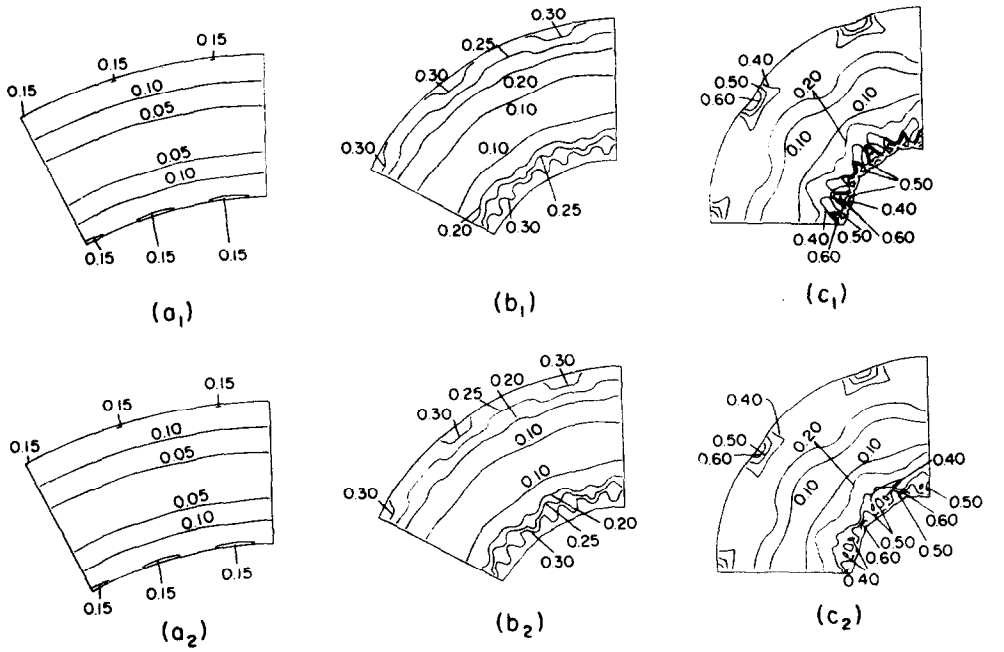

Fig. 6. Contours of constant maximum principal logarithmic strain in the deformed configuration (one half the plate is shown) for the two vertex characterizations employed here. (a) $\kappa h_0 = 0.31$, (b) $\kappa h_0 = 0.71$ and (c) $\kappa h_0 = 1.02$. The subscript 1 refers to the vertex characterized by $(\beta_c)_{max} = 135°$ and the subscript 2 refers to the vertex characterized by $(\beta_c)_{max} = 115°$. The initial imperfection is specified by $\bar{\xi}_1 = 0.0006$, $m_1 = 1$ and $\bar{\xi}_2 = 0$ in (8), with a half wavelength to initial thickness ratio of 0.301. The configuration shown is for a plate five wavelengths long, but only one half wavelength was analyzed numerically.

Figures 6(c) exhibit the fully developed shear band pattern for the two vertex characterizations. Although in Fig. 6(c_2), corresponding to the more blunt vertex, shear band development is significantly retarded compared to that exhibited in Fig. 6(c_1), certain qualitative features are common to both shear band patterns. For example, the greatest shearing occurs on the compressive side of the plate. The course of shear band development for the nonlinear elastic solid is quite different from that for the J_2 corner theory solids in that once shear bands do appear on the tensile side of the plate, relatively little additional growth of the shear bands on the compressive side takes place.

A common feature exhibited by both the J_2 corner theory solids and by the nonlinear elastic

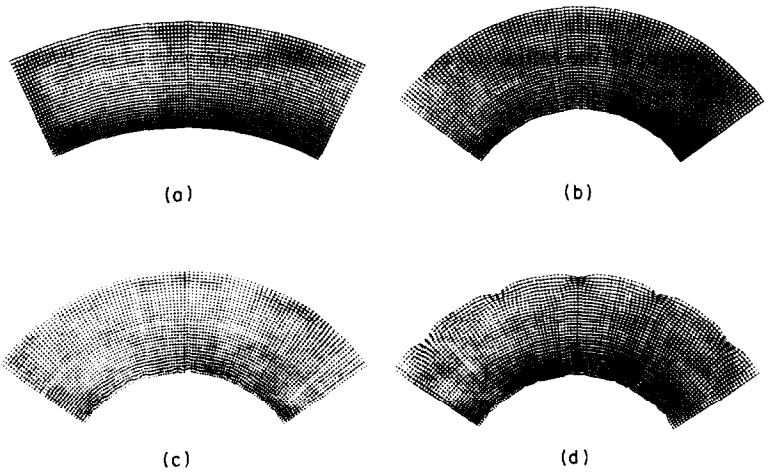

Fig. 7. The deformed mesh at four curvatures for the nonlinear elastic solid. (a) $\kappa h_0 = 0.300$, (b) $\kappa h_0 = 0.626$, (c) $\kappa h_0 = 0.632$ and (d) $\kappa h_0 = 0.654$. The initial imperfection is specified by $\bar{\xi}_1 = 0.0006$, $m = 1$ and $\bar{\xi}_2 = 0$ in (8), with a half wavelength to initial thickness ratio of 0.301. The configuration shown is for a plate five wavelengths long, but only one half wavelength was analyzed numerically.

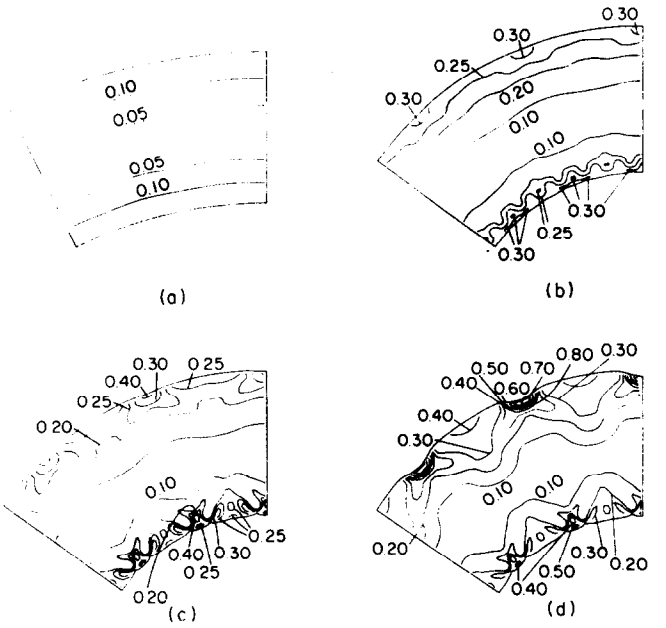

Fig. 8. Contours of constant maximum principal logarithmic strain in the deformed configuration (only one half the plate is shown) for the nonlinear elastic solid. (a) $\kappa h_0 = 0.300$, (b) $\kappa h_0 = 0.626$, (c) $\kappa h_0 = 0.632$ and (d) $\kappa h_0 = 0.654$. The initial imperfection is specified by $\bar{\xi}_1 = 0.0006$, $m_1 = 1$ and $\bar{\xi}_2 = 0$ in (8), with a half wavelength to initial thickness ratio of 0.301. The configuration shown is for a plate five wavelengths long, but only one half wavelength was analyzed numerically.

solid is that not every wave peak on the compressive side of the plate in Figs. 6(b) and 8(b) develops into a shear band.

In the results presented so far, attention has been confined to periodic imperfections and periodic deformation patterns. Quite general considerations, Tvergaard and Needleman[31], suggest that after the maximum moment has been attained, preferential growth of a localized pattern is to be expected. Figures 9–12 illustrate the effect of a long wavelength imperfection superposed on a shorter wavelength imperfection. Two imperfections of the form (8) are considered with one component having a half-wavelength of $L_0/5$. In one case $\bar{\xi}_1 = 0.0015$, $m_1 = 2$, $\bar{\xi}_2 = -0.0006$, $m_2 = 5$, which gives rise to the minimum thickness cross section occurring at $x^1/L_0 = 0.44$, while in the other case a larger imperfection giving the minimum cross section nearer $x^1 = 0$, at $x^1/L_0 = 0.17$ is specified, namely $\bar{\xi}_1 = -0.01$, $m_1 = 1$, $\bar{\xi}_2 = 0.0025$, $m_2 = 5$. In each case we confine our attention to the J_2 corner theory solid with the sharper of the two limiting cone angles considered, $(\beta_c)_{\max} = 135°$. A 32×48 finite element grid is employed, with the conditions on element orientation giving $L_0/h_0 = 1.45$.

Figure 9 displays the computed curves of nondimensional moment, $M/\sigma_y h_0^2$, vs the curvature parameter κh_0, as defined by (30). For the smaller imperfection the moment curvature relation

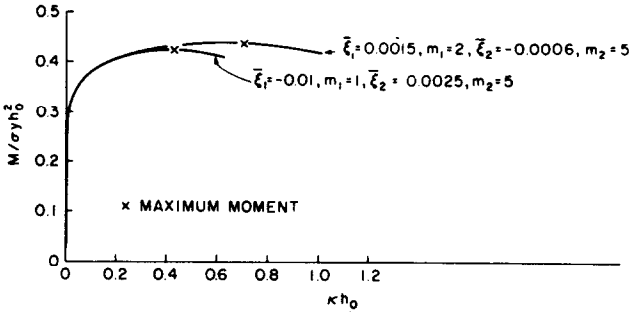

Fig. 9. The moment, M, vs curvature, κh_0, relations for plates with two different imperfections. In each case $L_0/h_0 = 1.45$ and the constitutive law employed is the J_2 corner theory with $(\beta_c)_{\max} = 135°$.

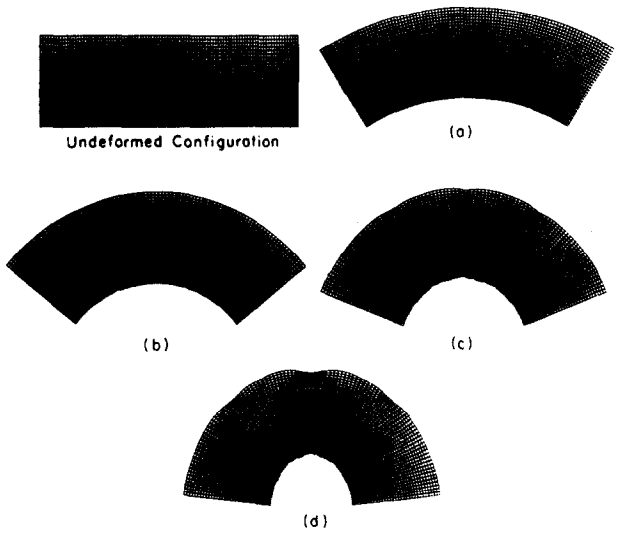

Fig. 10. The undeformed configuration and the deformed mesh at four curvatures for J_2 corner theory with $(\beta_c)_{max} = 135°$, $L_0/H_0 = 1.45$, and $\bar{\xi}_1 = 0.0015$, $m_1 = 2$, $\bar{\xi}_2 = -0.0006$ and $m_2 = 5$ in (8). (a) $\kappa h_0 = 0.38$, (b) $\kappa h_0 = 0.62$, (c) $\kappa h_0 = 0.83$ and (d) $\kappa h_0 = 1.01$.

hardly differs from the corresponding one in Fig. 4, despite the presence of a longer wavelength imperfection with an amplitude two and a half times greater than the imperfection with $m_2 = 5$. The maximum moment occurs at a slightly smaller curvature, $\kappa h_0 = 0.71$ in Fig. 9 as compared with $\kappa h_0 = 0.72$ in Fig. 4, while the value of the maximum moment itself is virtually unaltered. However, consistent with the considerations of [31], the moment decreases more rapidly when localization occurs, Fig. 9, than when the deformations remain periodic, Fig. 4. For the larger imperfection, the location as well as the value of the maximum moment are significantly altered.

Figures 10–13 depict the deformation patterns at four stages of loading. For comparison purposes Figs. 10 and 12 also show the undeformed configurations for each of the imperfection patterns considered. The symmetry about $x^1 = 0$ exhibited in Figs. 10 and 12 is enforced by the boundary conditions; only one half of the mesh is employed in the computations.

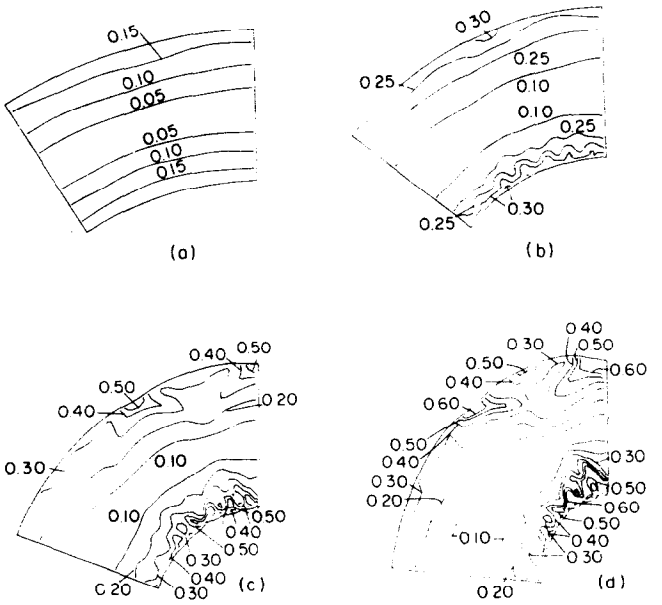

Fig. 11. Contours of constant maximum principal logarithmic strain in the deformed configuration (one half the plate is shown) for J_2 corner theory with $(\beta_c)_{max} = 135°$, $L_0/h_0 = 1.45$, and $\bar{\xi}_1 = 0.0015$, $m_1 = 2$, $\bar{\xi}_2 = -0.0006$ and $m_2 = 5$ in (8). (a) $\kappa h_0 = 0.38$, (b) $\kappa h_0 = 0.62$, (c) $\kappa h_0 = 0.83$ and (d) $\kappa h_0 = 1.01$.

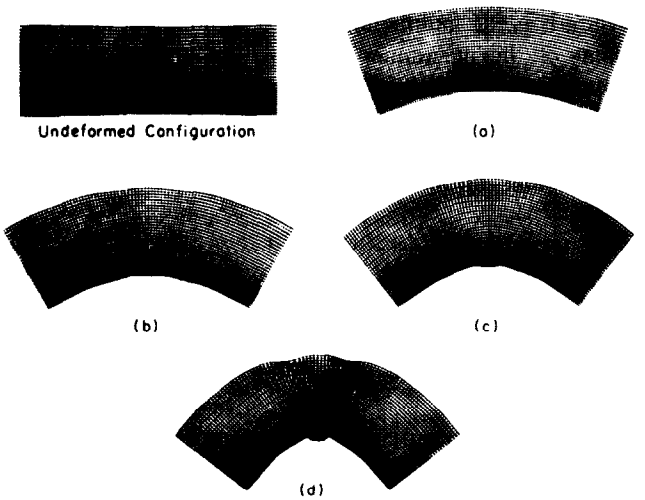

Fig. 12. The undeformed configuration and the deformed mesh at four curvatures for J_2 corner theory with $(\beta_c)_{max} = 135°$, $L_0/h_0 = 1.45$, and $\bar{\xi} = -0.01$, $m_1 = 1$, $\bar{\xi}_2 = 0.0025$ and $m_2 = 5$ in (8). (a) $\kappa h_0 = 0.24$, (b) $\kappa h_0 = 0.36$, (c) $\kappa h_0 = 0.46$ and (d) $\kappa h_0 = 0.63$.

In Figs. 10 and 11 where results are displayed for the smaller of these two imperfections, the first two stages of deformation shown are on the ascending branch of the moment-curvature curve and the deformation pattern is nearly periodic with period $L_0/5$, although indications of the influence of the longer wavelength imperfection can be seen. The more localized shear band pattern that has emerged is evident in the latter two stages shown. The greatest shearing has occurred on the symmetry line $x^1 = 0$ at the compressed surface of the plate, even though this is not initially the minimum thickness cross section. The contour plots in Figs. 11(c) and (d) show evidence of regions of shearing induced by the shorter wavelength imperfections that have not developed as the deformation have become more concentrated into the pattern favored by the long wavelength imperfection.

The development of the deformation pattern depicted in Figs. 12 and 13 for the larger imperfection differs from the previous ones shown. This imperfection is visible in the un-

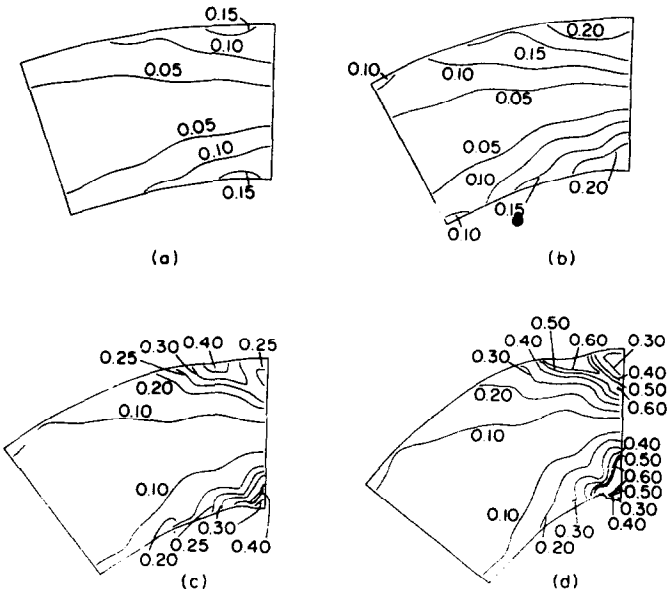

Fig. 13. Contours of constant maximum principal logarithmic strain in the deformed configuration (one half the plate is shown) for J_2 corner theory with $(\beta_c)_{max} = 135°$, $L_0/h_0 = 1.45$, and $\bar{\xi}_1 = -0.01$, $m_1 = 1$, $\bar{\xi}_2 = 0.0025$ and $m_2 = 5$ in (8). (a) $\kappa h_0 = 0.24$, (b) $\kappa h_0 = 0.36$, (c) $\kappa h_0 = 0.46$ and (d) $\kappa h_0 = 0.63$.

deformed mesh shown in Figs. 12 and the long wavelength imperfection clearly manifests itself prior to the attainment of the maximum moment. No surface wave development can be detected on the compressive side of the plate prior to the formation of shear bands. On the contrary, the initial waviness of this surface appears to flatten out somewhat. However, within the highly developed shear band evident in Figs. 12(d) and 13(d) there are very short wavelength surface oscillations on the compressed surface.

6. DISCUSSION

The shear bands exhibited in Figs. 5(c), 10(d) and 12(d) for a strain hardening elastic–plastic solid with a vertex on the yield surface are arranged in a pattern which resembles that associated with the formation of a plastic hinge. The location, and number, of these "plastic hinges" varies but the pattern of shear bands forming the hinge is qualitatively similar in each figure.

The shear bands originate at strain concentrations on the plate surfaces, induced by the initial thickness inhomogeneity. Here the short wavelength component of the thickness imperfection ($m = 5$) plays the primary role in developing these surface strain concentrations. When longer wavelength imperfections are present, as in Figs. 10 and 12, their main effect is to favor the development of one or more particular plastic hinges. The initial short wavelength surface waviness can amplify into a considerable surface roughness prior to shear band development, particularly on the compressive side of the plate. However, if the initial imperfection gives a more pronounced local thickness reduction, as in Fig. 12, then shear bands can form without substantial growth of the surface undulations occurring first.

The course of shear band development in pure bending can be compared with that found in plane strain tension specimens with initial thickness inhomogeneities by Tvergaard *et al.*[5]. In plane strain tension[5], as here, the shear bands intersect the free surface at points of strain concentration induced by the initial thickness imperfections. However, in plane strain tension, due to diffuse necking, the most intense straining prior to shear band formation occurs in the interior of the specimen. For the J_2 corner theory solid, this leads to intense shearing taking place in the interior of the specimen and in certain circumstances, permits internal shear bands unconnected to the free surfaces to form[5]. On the other hand, in pure bending, the shear bands must propagate inward against an adverse deformation gradient. The peak straining within the shear bands always occurs at the free surfaces. Furthermore, due to this deformation gradient the shear bands exhibited here are clearly curved compared with the essentially straight shear bands found in [5]. The shear bands end inside the material, although as can be seen in the contour plots, Figs. 6, 8, 11 and 13, their presence has an effect on strain contours still in the elliptic regime.

The present results show a significant dependence of the course of shear band development on the constitutive law employed to characterize the material behavior. The two vertex characterizations employed here were also employed by Hutchinson and Tvergaard[12] in their study of shear band development in plane strain tension. For the sharper vertex, $(\beta_c)_{\max} = 135°$, all straining eventually localized in the shear band, while the more blunt vertex, $(\beta_c)_{\max} = 115°$, led to a saturation of localized deformation within the shear band with the most critical initial orientation except for a very large imperfection[12]. For the more blunt vertex localization did occur with small imperfections although in shear bands not in the initial orientation optimal for bifurcation and at a somewhat higher strain level. The difference between these vertex descriptions manifests itself when the deviation from proportional loading is such that total loading no longer takes place. During the initial phases of surface wave growth, even up to $\kappa h_0 = 0.71$ in Figs. 5 and 6, the deviation from proportional loading, at the surfaces, is not great enough for there to be a large difference between the response of these two J_2 corner theory solids. However, shear band development necessitates large deviations from proportional loading and in Figs. 5 and 6 shear band development is visibly retarded for the solid with the more blunt vertex. For the classical elastic plastic solid with a smooth yield surface the response to a change in loading path is so stiff that shear bands would not form at the strain levels encountered here.

The response of the nonlinear elastic solid is more complex than that of either J_2 corner theory solid. As the shear bands form on the compressive side of the plate, the curvature

decreases as shown in Fig. 5. This "snap-back" in curvature is analogous to, but more complicated than, that found for a nonlinear elastic solid by Tvergaard *et al.*[5] in plane strain tension. Due to the adverse deformation gradient, the shear band growth on the compressive side of the plate is limited. Straining continues on the tensile side of the plate under increasing curvature. Subsequently, with the formation of shear bands on the tensile side of the plate the second "snap-back" of curvature is encountered.

The shear band pattern that develops in the nonlinear elastic solid, Figs. 7 and 8, consequently differs from those shown for the J_2 corner theory solids in Figs. 5 and 6. Considering the "soft" response of the nonlinear elastic solid to a change in loading path there is relatively little penetration of the shear bands on the compressive side of the plate into the center. On the other hand, comparing Figs. 6 and 8, the nonlinear elastic solid exhibits greater straining along the tensile surface. These features are related and are associated with the stress relaxation that occurs outside the shear bands with increasing deformation in the bands.

For all cases considered, in which the deformation pattern is required to remain periodic, the concentration of deformation into the shear bands occurs rather slowly. An additional long wavelength imperfection significantly enhances the concentration of deformation into shear bands as can be seen by a comparison of Figs. 5 and 6 with Figs. 10 and 11, even though the long wavelength imperfection itself does not appear to grow substantially. Somewhat beyond the maximum moment a localized deformation pattern rather than a periodic one is preferred, as discussed by Tvergaard and Needleman[31] in the context of localization of buckling patterns. In more general situations than the pure bending problem considered here, when shear bands must propagate against an adverse deformation gradient, this mechanism which focusses the deformation into one or a few shear bands may enhance shear band growth significantly.

As in the plane strain tension problem considered by Tvergaard *et al.*[5] the question arises as to the relationship between the discretized problem we have solved and the corresponding continuum problem. In [5], the importance of an appropriate mesh orientation for resolving shear bands was discussed. Since the shear bands in [5] were essentially straight lines, a near optimum mesh orientation could be employed across the specimen. Here, due to the curvature of the shear bands induced by the strongly nonuniform pre-shear band deformation state an optimum grid orientation throughout the plate is not feasible. Undoubtedly, this leads to some mesh induced shear band broadening as discussed by Tvergaard *et al.*[5]. Mesh induced or not, the finite width of the shear bands precludes a direct comparison of the shear band orientations here with the characteristic curves shown in the surface hyperbolic regimes in pure bending by Triantafyllidis[9].

In one respect, at least, the relation between the present discretized results and the underlying continuum results is less problematical than in [5]. For the J_2 corner theory solid, it was found in [5] that the core of the neck continued to deform after shear band formation and internal shear bands could form in this region. In the discretized problem the separation of these internal bands was set by the mesh spacing whereas in the continuum problem there is no natural length scale to set a minimum width of bands or a minimum separation between bands. In pure bending due to the adverse deformation gradient there is no tendency for such internal bands to form. This problem of material dependent length scales does, however, arise in another guise. Intense surface oscillations occur where the shear bands meet the free surface on the compressive side of the plate. Here, the minimum possible wavelength of these oscillations is set by the mesh spacing, whereas in a real material some natural length scale would limit this wavelength. By way of contrast, on the tensile side of the plate the surface and a deep relatively wide depression forms. On the tensile side there is no tendency for a surface undulation with the shortest wavelength permitted by the mesh to form.

The present results suggest that in pure bending of a plate made of a material prone to shear band development, the notch-like protuberances on the compressive side of the plate would serve as likely failure initiation sites. In practice, pure bending is rarely, if ever, encountered. If the compressive strain at the free surface is reduced, either by the restraint arising from contact with a die surface or by a combination of imposed bending and stretching, the growth of these very short wavelength oscillations would be expected to be retarded, and fracture may occur first on the tensile side. In fact, surface shear fractures observed on the tensile side of bent plates[10], subsequent to the development of surface waviness, seem to agree with the shear

band development determined in the present study. A combination of bending and stretching would likely enhance the growth of the surface depressions on the tensile side.

Acknowledgments—This work was supported by the U.S. National Science Foundation through Grand ENG76-16421. The computations reported on here were carried out on the Brown University, Division of Engineering, VAX-11/780 computer. The acquisition of this computer was made possible by grants from the U.S. National Science Foundation (Grant ENG78-19378), the General Electric Foundation and the Digital Equipment Corporation.

REFERENCES

1. J. Hadamard, *Lecons sur la Propagation des Ondes et les Equations de L'Hydrodynamique* Paris (1903).
2. T. Y. Thomas, *Plastic Flow and Fracture of Solids*. Academic Press, New York (1961).
3. R. Hill, Acceleration waves in solids. *J. Mech. Phys. Solids* **10**, 1 (1962).
4. J. R. Rice, The localization of plastic deformation. *Proc. 14th Int. Congr. Theor. and Appl. Mech.* (Edited by W. T. Koiter), p. 207. North-Holland, Amsterdam (1976).
5. V. Tvergaard, A. Needleman and K. K. Lo, Flow localization in the plane strain tensile test. *J. Mech. Phys. Solids*, **29**, 115 (1981).
6. R. Abeyaratne and N. Triantafyllidis, On the emergence of shear bands in plane strain. *Materials Res. Lab. Rep. MRL E-125*. Brown University, July (1980). Also *Intl. J. Solids & Structures* (in press).
7. J. K. Knowles and E. Sternberg, Discontinuous deformation gradients near the tip of a crack in finite anti-plane shear: an example. *J. Elasticity* **10**, 81 (1980).
8. R. Abeyaratne, Discontinuous deformation gradients away from the tip of a crack in anti-plane shear. *J. Elasticity* **10**, 255 (1980).
9. N. Triantafyllidis, Bifurcation phenomena in pure bending. *J. Mech. Phys. Solids* **28**, 221 (1980).
10. J. W. Hutchinson and V. Tvergaard, Surface instabilities on statically strained plastic solids. *Int. J. Mech. Sci.* **22**, 339 (1980).
11. J. Christoffersen and J. W. Hutchinson, A class of phenomenological corner theories of plasticity. *J. Mech. Phys. Solids* **27**, 465 (1979).
12. J. W. Hutchinson and V. Tvergaard, Shear band formation in plane strain. *Int. J. Solids Structures*, **17**, 451 (1981).
13. J. W. Rudnicki and J. R. Rice, Conditions for the localization of deformation in pressure-sensitive dilatant materials. *J. Mech. Phys. Solids* **23**, 371 (1975).
14. B. Budiansky, Remarks on theories of solid and structural mechanics. *Problems of Hydrodynamics and Continuum Mechanics*, p. 77. Society for Industrial and Applied Mathematics (1969).
15. A. E. Green and W. Zerna, *Theoretical Elasticity*. Oxford University Press (1968).
16. A. Needleman, A numerical study of necking in circular cylindrical bars. *J. Mech. Phys. Solids* **20**, 111 (1972).
17. V. Tvergaard, Effect of thickness inhomogeneities in internally pressurized elastic-plastic spherical shells. *J. Mech. Phys. Solids* **24**, 291 (1976).
18. A. Needleman and V. Tvergaard, Necking of biaxially stretched elastic-plastic circular plates. *J. Mech. Phys. Solids* **25**, 159 (1977).
19. R. Hill, The essential structure of constitutive laws for metal composites and polycrystals. *J. Mech. Phys. Solids* **15**, 79 (1967).
20. J. W. Hutchinson, Elastic-plastic behavior of polycrystalline metals and composites. *Proc. Roy. Soc. London* A318, 247 (1970).
21. T. H. Lin, Physical theory of plasticity. *Adv. Appl. Mech.* **11**, 255 (1971).
22. S. S. Hecker, Experimental studies of yield phenomena in biaxially loaded metals. *Constitutive Equations in Viscoplasticity* AMD Vol. 20, p. 1, ASME (1976).
23. S. B. Batdorf, Theories of plastic buckling. *J. Aeronaut. Sci.* **16**, 405 (1949).
24. J. W. Hutchinson, Plastic buckling. *Adv. Appl. Mech.* **14**, 67 (1974).
25. R. Hill, Some aspects of the incremental behaviour of isotropic elastic solids after finite strain. *Problems in Mechanics: Deformation of Solid Bodies*, p. 459. Leningrad (1969).
26. R. Hill, Constitutive inequalities for isotropic elastic solids under finite strain. *Proc. Roy. Soc. Lond.* **A314**, 457 (1970).
27. R. Hill, Aspects of invariance in solid mechanics. *Adv. Appl. Mech.* **18**, 1 (1978).
28. S. Storen and J. R. Rice, Localized necking in thin sheets. *J. Mech. Phys. Solids* **23**, 421 (1975).
29. N. Triantafyllidis, Bending effects in sheet metal forming. Ph.D. Thesis. Brown University (1980).
30. R. Rivlin, Large elastic deformations of isotropic materials VI, further results in the theory of torsion, shear and flexure. *Phil. Trans. Roy. Soc. Lond.* **A242**, 173 (1949).
31. V. Tvergaard and A. Needleman, On the localization of buckling patterns, *J. Appl. Mech.* **47**, 613 (1980).